GEOPHYSICS, VOL. 66, NO. 3 (MAY-JUNE 2001); P. 836–844, 11 FIGS., 1 TABLE.

Discrimination between pressure and fluid saturation changes from time-lapse seismic data

Martin Landrø*

ABSTRACT

Explicit expressions for computing saturation- and pressure-related changes from time-lapse seismic data have been derived and tested on a real time-lapse seismic data set. Necessary input is near- and far-offset stacks for the baseline seismic survey and the repeat survey. The method has been tested successfully in a segment where pressure measurements in two wells verify a pore-pressure increase of 5 to 6 MPa between the baseline survey and the monitor survey. Estimated pressure changes using the proposed relationships fit very well with observations. Between the baseline and monitor seismic surveys, 27% of the estimated recoverable hydrocarbon reserves were produced from this segment. The estimated saturation changes also agree well with observed changes, apart from some areas in the water zone that are mapped as being exposed to saturation changes (which is unlikely). Saturation changes in other segments close to the original oil–water contact and the top reservoir interface are also estimated and confirmed by observations in various wells.

INTRODUCTION

Predicting overpressured zones from seismic data has been tested and reported by several researchers [e.g., Reynolds (1970) and Bilgeri and Ademeno (1982)]. The basic tool in such studies has been velocity analysis. By detecting areas where the estimated velocities deviate from the normal trend, Martinez et al. (1991) estimate acoustic impedances by seismic inversion; velocities and densities are then estimated using a relationship between sonic velocities and acoustic impedances. However, for most reservoirs, pressure changes in combination with fluid-saturation changes create abnormal seismic responses. It is often difficult to separate the two effects from seismic data only. In most time-lapse seismic studies, seismic differences between a baseline and a monitor survey are analyzed and interpreted as either a pressure effect or a fluid effect. In the Magnus 4-D study (Watts et al., 1996), the main seismic changes were attributed to pore-pressure changes, while in the Gullfaks (Landrø et al., 1999) and the Draugen (Gabriels et al., 1999) 4-D seismic studies, most of the seismic changes were interpreted as fluid related. However, for some fields or segments within a field, both fluid and pressure changes have approximately the same degree of impact on the seismic data. In such cases the use of time-lapse amplitude variation with offset (AVO) analysis offers an opportunity to discriminate the two effects (Tura and Lumley, 1998, 1999a; Landrø, 1999). I describe a method to estimate fluid- and pressure-related changes directly from repeated near- and far-offset stacked data. I focus on a segment from the Gullfaks field, where the pore pressure increased by approximately 5–6 MPa (725-870 psi) because of water injection in the period between the baseline and the monitor surveys. In the same period 27% of the estimated recoverable hydrocarbon reserves were produced. For such a case, it is important and very useful to estimate two different maps instead of one—one for pressure-related changes and another for fluid saturation-related changes—by using the methodology presented in this paper.

Other production-related changes have impact on time-lapse seismic data, e.g., gas injection and temperature. However, I focus on discriminating between pore-pressure and fluid-saturation changes. [See also Brevik (1999), Tura and Lumley (1999b), and Landrø (1999).]

SATURATION AND PRESSURE VERSUS SEISMIC PARAMETERS

Distinguishing between fluid-saturation and pore-pressure changes from seismic data requires knowing how seismic parameters are influenced by such changes. In the Gullfaks 4-D project (Landrø et al., 1999) a rock physics model calibrated with well-log measurements was used to predict the seismic effect of substituting oil with water. The basic equation in the rock physics model is the Gassmann equation (Gassmann, 1951). Repeated logging in wells typically shows a change in

Manuscript received by the Editor December 2, 1998; revised manuscript received August 22, 2000.
*Formerly Statoil Research Centre, Trondheim, Norway. Presently Norwegian University of Science and Technology, Department of Petroleum Technology and Applied Geophysics, N-7491 Trondheim, Norway. E-mail: mlan@ipt.ntnu.no.

water saturation from values around 10% (preproduction) to around 70% to 80% (postproduction). The relationship between saturation changes and *P*-wave velocity after calibrating the Gassmann model to some of the wells at the Gullfaks field is shown in Figure 1. The relationship is nonlinear, but not strongly so. To the first order, I therefore assume the relationship between seismic parameters and saturation changes can be approximated by linear functions at Gullfaks.

The common way to obtain a relationship between seismic parameters and pressure changes is to perform ultrasonic measurements on several cores taken from various formations. A typical curve for *P*-wave velocity versus effective pressure changes is displayed in Figure 2. This curve represents the average of 29 core measurements from the Gullfaks field. The Gullfaks reservoir rock is of early and middle Jurassic age, representing shallow marine to fluvial deposits. The reservoir depth is approximately 2000 m. The initial pore pressure is 32 MPa, and the overburden pressure is approximately 38 MPa. Typical porosities are around 30%. All measurements were made on dry core samples. Comparison of dry and brine-saturated acoustic core measurements shows that the compressional velocities are higher in brine-saturated rock. The saturation effect is more pronounced at lower net pressures (Winkler, 1985). The net pressure is equal to the overburden pressure (or stress) minus the pore pressure. This means a pore pressure increase will decrease net pressure. In comparison with the velocity versus saturation curve shown in Figure 1, the curve in Figure 2 is highly nonlinear. As will be shown later, this nonlinear behavior requires a second-order approximation of the relationship between seismic parameters and pressure changes. A summary of the rock physics feasibility study for Gullfaks is shown in Figure 3.

Regarding the curves in Figures 1 and 2, I posed two questions: Is it valid to compare velocities measured at high frequencies with seismic velocities, and is it valid to compare pressure measurements made on a dry core sample that has gone through reloading and loading several times with the stress conditions actually taking place in the reservoir rock? Despite these concerns, I used numerical figures obtained from the rock physics study as a link between reservoir production changes and seismic changes.

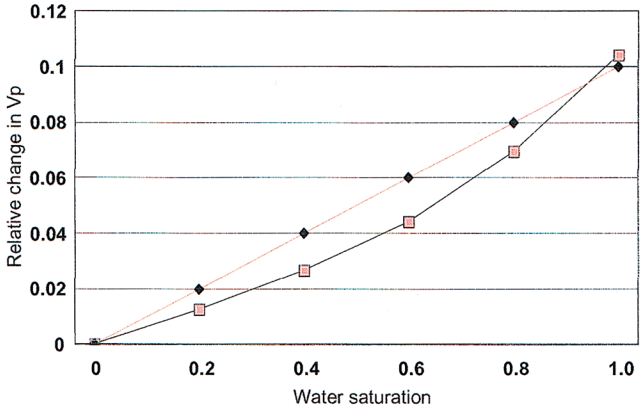

FIG. 1. Typical modeled relationship between relative change in *P*-wave velocity and water saturation (line with squares). The curve is based upon a calibrated Gassmann model. The line with diamonds shows the straight-line approximation used in the real data example.

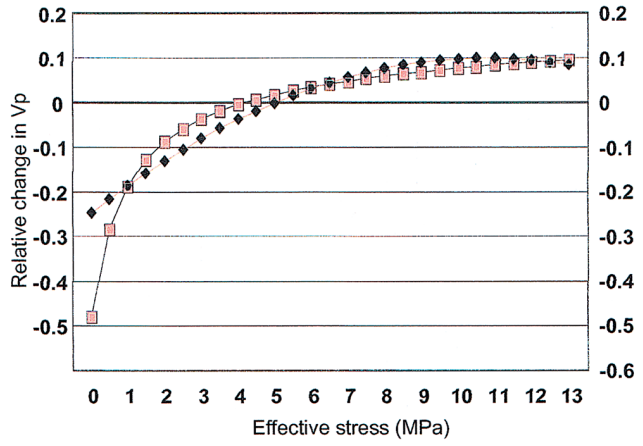

FIG. 2. Relative *P*-wave velocity changes versus changes in net pressure (line with squares). Initial net pressure at Gullfaks is assumed to be around 5 to 6 MPa, and expected changes in net pressure might range from −5 MPa (for a pore-pressure increase) to +5 MPa (for a pore-pressure decrease). The diamond line shows the approximated second-order approximation used in the real data example.

METHODOLOGY

One way to estimate several production-related parameters simultaneously is to increase the number of independent seismic measurements. The first approach for achieving this using conventional seismic data is to exploit the AVO and regard the near- and far-offset stacks as independent measurements. Another approach is to use shear-wave seismic data—for instance, a *PS*-converted stack. In the present case, I use the first approach, mainly because no *PS*-converted time-lapse data are available at Gullfaks.

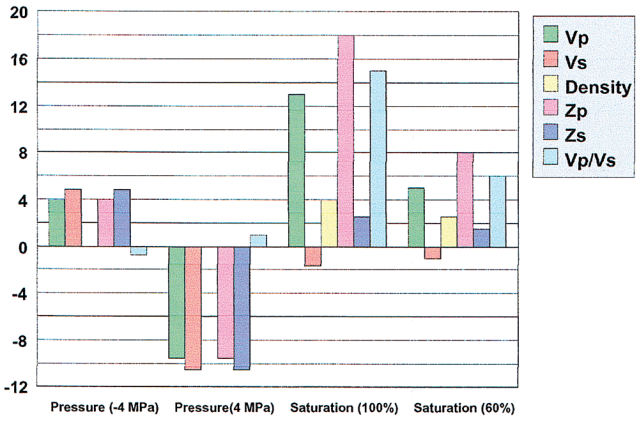

FIG. 3. Expected changes in various seismic parameters from changes in pore pressure and water saturation; 60% change in water saturation means from 20% to 80%. Z_p and Z_s denote *P*- and *S*-wave impedances, respectively. Average porosity is 30%, initial pore pressure is 32 MPa, and reservoir depth is approximately 2000 m. (Figure reprinted with permission from Petroleum Geoscience.)

Let us consider a two-layer model: a cap-rock layer (layer 1, shale) above a reservoir layer (layer 2, sand). For simplicity we will first study the situation when only fluid-saturation changes occur in layer 2; next, we will study only pressure changes in layer 2. We assume the P-wave velocity in layer 1 (α_1) remains constant between the baseline and the repeated survey, as well as for the S-wave velocity (β_1) and the density (ρ_1). In layer 2 (which is assumed to be the porous reservoir layer) the preproduction parameters are denoted α_2, β_2, etc. The same parameters after fluid substitution in layer 2 are denoted α_2', β_2', etc. The lithological parameter contrast in P-wave velocity is $\Delta\alpha = \alpha_2 - \alpha_1$, while the parameter contrast from fluid changes in layer 2 can be expressed as $\Delta\alpha^F = \alpha_2' - \alpha_2$ or, more precisely,

$$\Delta\alpha^F = \alpha_2[S_W(t_2)] - \alpha_2[S_W(t_1)], \tag{1}$$

where S_W denotes water saturation; t_1 and t_2 denote the timing for the baseline and monitor seismic surveys, respectively; and subscript 2 of α_2, etc., refers to layer 2. The reflection coefficient prior to production is [assuming the Smith and Gidlow (1987) approximation]

$$R_0(\theta) = \frac{1}{2}\left(\frac{\Delta\rho}{\rho} + \frac{\Delta\alpha}{\alpha}\right) - \frac{2\beta^2}{\alpha^2}\left(\frac{\Delta\rho}{\rho} + \frac{2\Delta\beta}{\beta}\right)\sin^2\theta + \frac{\Delta\alpha}{2\alpha}\tan^2\theta, \tag{2}$$

where $\alpha = (\alpha_1 + \alpha_2)/2$, etc. After fluid substitution in layer 2, we find the postproduction reflection coefficient as

$$R_1(\theta) = \frac{1}{2}\left(\frac{\Delta\rho'}{\rho'} + \frac{\Delta\alpha'}{\alpha'}\right) - \frac{2\beta'^2}{\alpha'^2}\left(\frac{\Delta\rho'}{\rho'} + \frac{2\Delta\beta'}{\beta'}\right)\sin^2\theta + \frac{\Delta\alpha'}{2\alpha'}\tan^2\theta. \tag{3}$$

In equation (3), $\Delta\alpha' = \alpha_2' - \alpha_1 = \alpha_2 + \Delta\alpha^F - \alpha_1 = \Delta\alpha + \Delta\alpha^F$, etc. Correspondingly, $\alpha' = (\alpha_1 + \alpha_2 + \Delta\alpha^F)/2 = \alpha(1 + (\Delta\alpha^F/2\alpha))$, etc. Assuming that $\Delta\alpha/\alpha \ll 1$ and $\Delta\alpha^F/\alpha \ll 1$ and neglecting higher-order terms in either $\Delta\alpha/\alpha$ or $\Delta\alpha^F/\alpha$ or combinations of them, we obtain

$$R_1(\theta) = \frac{1}{2}\left(\frac{\Delta\rho}{\rho} + \frac{\Delta\alpha}{\alpha}\right) - \frac{2\beta^2}{\alpha^2}\left(\frac{\Delta\rho}{\rho} + \frac{2\Delta\beta}{\beta}\right)\sin^2\theta + \frac{\Delta\alpha}{2\alpha}\tan^2\theta + \frac{1}{2}\left(\frac{\Delta\rho^F}{\rho} + \frac{\Delta\alpha^F}{\alpha}\right) - \frac{2\beta^2}{\alpha^2}\left(\frac{\Delta\rho^F}{\rho} + \frac{2\Delta\beta^F}{\beta}\right)\sin^2\theta + \frac{\Delta\alpha^F}{2\alpha}\tan^2\theta. \tag{4}$$

Equation (4) uses the following approximation for the velocity ratio term:

$$\frac{\beta'}{\alpha'} = \frac{\beta\left(1 + \frac{\Delta\beta^F}{2\beta}\right)}{\alpha\left(1 + \frac{\Delta\alpha^F}{2\alpha}\right)} \approx \frac{\beta}{\alpha}. \tag{5}$$

The delta terms in this velocity ratio $[(\Delta\beta^F/2\beta), (\Delta\alpha^F/2\alpha)]$ are to be multiplied with other delta terms inside the brackets of equation (4), $[(\Delta\rho/\rho) + (2\Delta\beta/\beta)]$. Since they will give second-order terms, they can be neglected. A detailed derivation including second-order terms is found in Appendix A. Furthermore, for fluid substitution one can assume that the shear modulus remains constant, provided the $\sin^2\theta$ term in equation (4) does not change under fluid substitution. This can be seen in the following way: Keeping the shear modulus constant means that $\beta^2\rho$ is constant, leading to the result that $[(\Delta\rho^F/\rho) + (2\Delta\beta^F/\beta)] = 0$ for fluid substitution. For fluid substitution, equation (4) therefore reads

$$R_1(\theta) \approx R_0(\theta) + \frac{1}{2}\left(\frac{\Delta\rho^F}{\rho} + \frac{\Delta\alpha^F}{\alpha}\right) + \frac{\Delta\alpha^F}{2\alpha}\tan^2\theta, \tag{6}$$

which again means that the change in reflectivity (to the lowest order) because of fluid saturation change in layer 2 is

$$\Delta R^F(\theta) \approx \frac{1}{2}\left(\frac{\Delta\rho^F}{\rho} + \frac{\Delta\alpha^F}{\alpha}\right) + \frac{\Delta\alpha^F}{2\alpha}\tan^2\theta. \tag{7}$$

A numerical example (Appendix B) testing the differences between using this approximate expression for reflectivity changes and using the exact equations shows a deviation in reflectivity of 4% at zero incidence angle and 1% at a 30° angle.

For pressure changes it is reasonable to assume that the density remains practically unchanged. We assume that the density can be written as

$$\rho = \phi\rho_f + (1 - \phi)\rho_s, \tag{8}$$

where ϕ is the porosity and ρ_f and ρ_s are the fluid and matrix densities, respectively. For a sandstone reservoir, the changes in porosity attributable to pressure changes are generally small; hence, the changes in density from pressure changes are also negligible. This is confirmed by the core measurement results shown in Figure 3. A corresponding equation for the reflectivity change because of a change in pore pressure (P) can therefore be approximated (again to the lowest order) by

$$\Delta R^P(\theta) \approx \frac{1}{2}\frac{\Delta\alpha^P}{\alpha} - \frac{4\beta^2}{\alpha^2}\frac{\Delta\beta^P}{\beta}\sin^2\theta + \frac{\Delta\alpha^P}{2\alpha}\tan^2\theta. \tag{9}$$

A reasonable assumption for relative variation of the seismic parameters with respect to fluid-saturation and pore-pressure changes can be written (using first-order expansion with respect to saturation changes and second-order expansion with respect to pressure changes)

$$\frac{\Delta\alpha}{\alpha} \approx k_\alpha\Delta S + l_\alpha\Delta P + m_\alpha\Delta P^2, \tag{10}$$

$$\frac{\Delta\beta}{\beta} \approx k_\beta\Delta S + l_\beta\Delta P + m_\beta\Delta P^2, \tag{11}$$

$$\frac{\Delta\rho}{\rho} \approx k_\rho\Delta S, \tag{12}$$

where ΔS and ΔP denote the changes in oil saturation and net pressure, respectively, and where k_α, k_β, k_ρ, l_α, l_β, m_α, m_β are empirical parameters estimated from, for instance, the saturation change curve in Figure 1 or the pressure change curve in Figure 2. The assumptions given in equations (10)–(12) are a reasonable approximation for the Gullfaks field. For other

fields with different reservoir properties, more advanced approximations might be necessary. These parameters are generally spatial variant. In practice, however, it is impossible to measure these parameters at all positions in space. Therefore, a realistic approach would be to estimate one parameter set for each formation or to assume that one average parameter set is representative of the whole field. As an example, the P-wave velocity increase (based on the average curve shown in Figure 1) as the result of a pore-pressure decrease of 4 MPa was estimated to 4% with a standard deviation of 1.5%. The standard deviation was computed on the basis of all 29 core samples used in the Gullfaks 4-D study. Here, I assume only one parameter set is valid for the whole field. The total change in reflectivity from the combined effect of fluid and pressure changes can thus be written

$$\begin{aligned}\Delta R \approx{}& \frac{1}{2}\left(k_\rho \Delta S + k_\alpha \Delta S + l_\alpha \Delta P + m_\alpha \Delta P^2\right)\\ &+ \frac{1}{2}\left(k_\alpha \Delta S + l_\alpha \Delta P + m_\alpha \Delta P^2\right)\tan^2\theta\\ &- \frac{4\beta^2}{\alpha^2}\left(l_\beta \Delta P + m_\beta \Delta P^2\right)\sin^2\theta. \end{aligned} \tag{13}$$

Using the conventional formula for the AVO intercept and gradient, $R = R_0 + G\sin^2\theta$, and assuming that $\tan^2\theta \approx \sin^2\theta$, equation (13) can be split into one intercept and one gradient term:

$$\Delta R_0 \approx \frac{1}{2}\left(k_\alpha \Delta S + k_\rho \Delta S + l_\alpha \Delta P + m_\alpha \Delta P^2\right), \tag{14}$$

$$\begin{aligned}\Delta G \approx{}& \frac{1}{2}\left(k_\alpha \Delta S + l_\alpha \Delta P + m_\alpha \Delta P^2\right)\\ &- \frac{4\beta^2}{\alpha^2}\left(l_\beta \Delta P + m_\beta \Delta P^2\right). \end{aligned} \tag{15}$$

These two equations can be solved to find explicit expressions for changes in pressure and water saturation. The solutions for the estimated pressure variation can be written

$$\Delta P \approx \frac{-b - \sqrt{b^2 - 4ac}}{2a}. \tag{16}$$

The negative root solution has been excluded since zero values for changes in intercept and gradient should give zero changes in pressure and saturation. This argument is only valid when b in equation (18) is positive, as it is in the present case, (If b is positive, which is very unlikely to happen for normal V_p/V_s ratios, one should choose the positive root solution instead.) The constants a, b, and c in equation (16) are

$$a = m_\alpha - \frac{8\beta^2}{\alpha^2}m_\beta - \frac{m_\alpha k_\alpha}{k_\alpha + k_\rho}, \tag{17}$$

$$b = l_\alpha - \frac{8\beta^2}{\alpha^2}l_\beta - \frac{k_\alpha l_\alpha}{k_\alpha + k_\rho}, \tag{18}$$

$$c = \frac{2k_\alpha \Delta R_0}{k_\alpha + k_\rho} - 2\Delta G, \tag{19}$$

which means they are expressed by the empirical constants, the V_p/V_s ratio, and the changes in intercept and gradient, as shown above.

The corresponding expression for saturation changes can be written as

$$\Delta S \approx \frac{1}{k_\alpha + k_\rho}\left(2\Delta R_0 - l_\alpha \Delta P - m_\alpha \Delta P^2\right). \tag{20}$$

Since we now have expressed the water-saturation change in terms of empirical parameters and changes in the intercept parameter (i.e., change in reflection coefficient at zero incidence angle) and the AVO gradient, we have obtained a direct way to distinguish between the two effects. The nice feature about these equations is that they represent a simple relation between water-saturation changes and parameters that can be estimated from time-lapse AVO data. It is of course possible to introduce other effects (such as temperature) into the formalism; but then we must also introduce a third AVO parameter, and it might be hard to estimate as many as three parameters for each CMP gather. Instead of estimating changes in the AVO intercept and gradient, we can also estimate changes in the near- and far-offset stacks and then convert these entities into changes in intercept and gradient.

Using the empirical relations for the Gullfaks field, I estimated $k_\alpha = 0.1$, $k_\beta = -0.03$, $k_\rho = 0.05$, $m_\alpha = -0.003$, $m_\beta = -0.003$, $l_\alpha = 0.035$, and $l_\beta = 0.035$. [The units of these parameters vary and are easily deduced from equations (10–12).] The quality of these parameter estimates is illustrated in Figures 1 and 2, where a comparison between the empirical relations and the measured (or calibrated) curves is shown. Using these values, I obtained the following expressions for saturation and pressure changes [assuming the V_p/V_s ratio is equal to 2 in equations (17) and (18)]:

$$\Delta S \approx 8(\Delta R_0 + \Delta G), \tag{21}$$

$$\Delta P \approx 23\Delta R_0 - 35\Delta G, \tag{22}$$

where the water saturation is measured as a fraction and the pore pressure is measured in megapascals. In the derivation of equations (21) and (22), I assumed all changes are small; hence, ΔR_0 and ΔG are much less than one. The scalars in equation (22) are measured in megapascals. A change in intercept of 0.04 and a gradient change of 0.01 will then correspond to a water-saturation change of 0.4 and a pore-pressure change of 0.6 MPa, for example. In deriving equations (21) and (22), I assumed that the production changes (either pressure or saturation) occurred in the layer below the interface. If the opposite is the case (for instance, for the oil–water contact), we get opposite signs in equations (7) and (9), which again means that both ΔR_0 and ΔG should have opposite signs. So when interpreting the estimated saturation-change and pressure-change cubes, we should remember that, for instance, an increase in water saturation for the top reservoir interface will appear as a water saturation decrease (negative ΔS values) at the oil–water contact. This effect is observed in Figure 7, where typical saturation changes associated with the top Brent reflector have opposite polarity of the changes close to the original oil–water contact at 1950 ms.

Figure 4 shows that the AVO curves obtained after 3-D prestack time migration often are heavily contaminated by noise. We must expect that the intercept and gradient term

estimates will be influenced by this noise. Because of the high noise level, the intercept and gradient sections were estimated directly from near- and far-offset stacks (which were less noise contaminated than the prestack gathers).

REAL DATA EXAMPLE

Time-lapse seismic data from the Gullfaks field were used to test the derived expressions for saturation and pressure changes. Details about the acquisition and processing parameters are found in Landrø et al. (1999). Figure 5 shows near- and far-offset partial stacks from seismic data acquired pre-production (1985) and after 10 years of production (1996). A scaling factor between near- and far-offset stacks was determined in the following way: The AVO response for the top Cretaceous and the top Brent interface was modeled, based on well logs. By comparing modeled near- to-far-offset ratios with measured ratios, a scalar was determined for each interface. This procedure was repeated for several wells. An average scalar was estimated and applied to the far-offset cube. Notice that the offset stacks from different acquisitions are quite similar for both nears and fars. The AVO effect for the top reservoir interface is also very clear on this display (Figure 5; compare the amplitude decrease for the top Cretaceous interface with the strong amplitude increase for the top reservoir interface). Despite the apparent similarities between 1985 and 1996 stacks, there are some distinct differences—

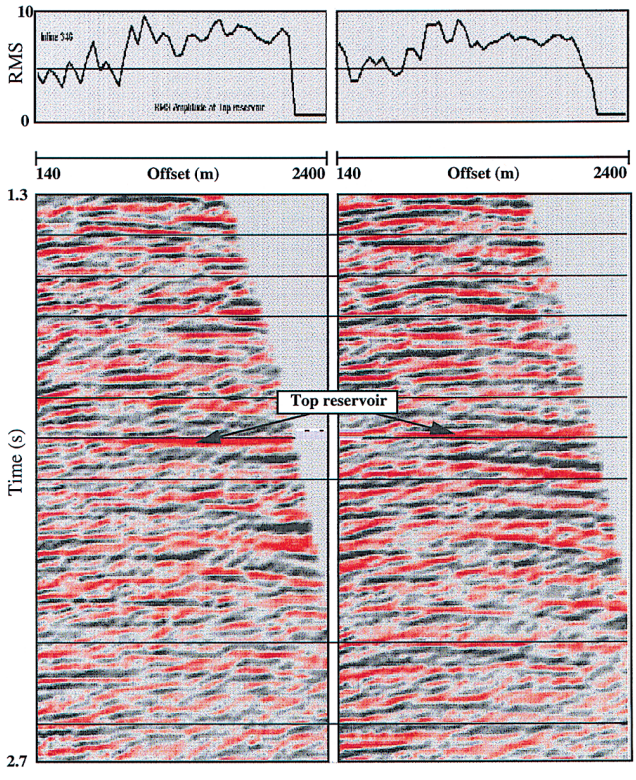

FIG. 4. Two bin gathers after 3-D prestack time migration, showing the AVO for the top reservoir reflector. Top reservoir amplitudes are shown at the top.

especially the increased amplitude for the top Cook interface. Another feature is the reduced reflectivity near the original oil–water contact from 1985 to 1996, especially on the far-offset stacks.

The offset ranges used to compute the partial stacks from different data sets were identical. Based on these near- and far-offset stacks, intercept (R_0) and gradient cubes were calculated (using simple assumption on average angle range covered by each stack). Then difference cubes for intercept and gradient were generated, as shown in Figure 6 for one in-line. Using the intercept and gradient difference cubes, the final step was to use the derived equations to obtain changes in saturation and pressure. Figure 7 shows an example of a seismic profile of saturation- and pressure-related changes. On the pressure attribute section, the pronounced amplitude difference at the top Cook interface is the most convincing feature.

Map views taken from the top Brent interface and the original oil–water contact of the saturation-related attribute cube

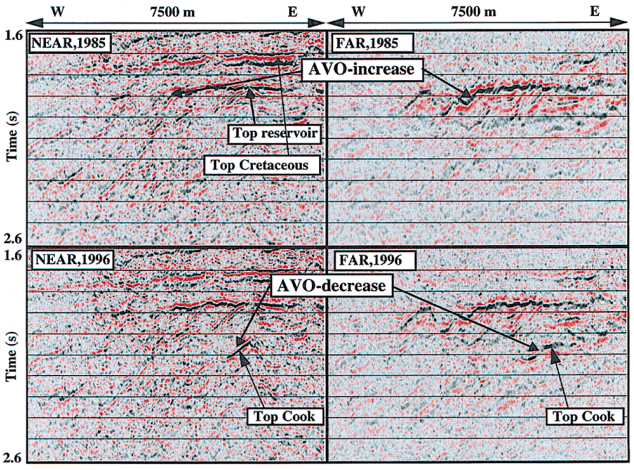

FIG. 5. Near- and far-offset stacks for the baseline survey (1985, top) and for the repeat survey (1996, bottom) for in-line 2760. The position of this line is shown in Figure 8. Notice the AVO increase at the flank of the reservoir (dipping event, marked with arrows) and the AVO decrease at the top Cook interface.

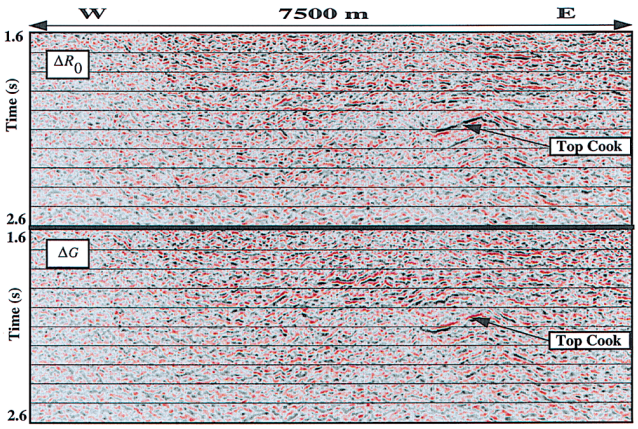

FIG. 6. Changes in intercept (R_0) and gradient (G) for the same seismic profile as shown in Figure 4 (in-line 2760, see Figure 8).

are shown in Figures 8 and 9, respectively. Both maps have saturation anomalies that agree well with observations. For instance, the anomaly north of injection well B-12 (visible on both maps) is interpreted as a water front emerging from the injector well toward the north. This was confirmed early in 1998 when the horizontal producer C-36 came onstream and encountered water in the southern part of the well track after a few weeks of production. Furthermore, the anomalies along the flank of the field have been confirmed by repeated saturation logging in these areas. Most of the anomalies shown in Figures 8 and 9 are also mapped on the difference cubes generated from the conventional stacked data.

A map view of the pressure anomaly at the top of the Cook is shown in Figure 10, together with the B-33 well path. This well started water injection in 1995 with a rate of 3000 m^3 per day. Water injection is believed to be the cause for the pressure buildup within this segment. Pressure measurements in this and a neighboring well show that the pore-pressure increase is 5–6 MPa. Measurements in the neighboring segment to the south show a significant pore-pressure decrease (on the order of 6 to 7 MPa), but no evidence for this can be found on the pressure attribute cube (Figure 10). This different behavior between a pore-pressure increase and decrease might be explained from Figure 2, where a pore-pressure increase (corresponding to a decrease in net pressure) results in a larger effect on the seismic velocities than a corresponding pore-pressure decrease of the same magnitude.

A detailed comparison between the fluid-saturation and the pore-pressure change attributes is shown in Figure 11. The extension of the pressure anomaly is restricted by faults. Fault-sealing analysis has been done on several faults at Gullfaks but not on the faults that appear as sealing with respect to pressure in Figure 11. In contrast, the fluid change anomaly seems to terminate close to the original oil–water contact, apart from the northern part of the segment. This is similar to the top Brent fluid-saturation map shown in Figure 8, where the anomalies follow the original oil–water contact. In 1996, 27% of the estimated reserves had been produced from this segment, so we expect to observe some fluid changes, especially in the neighborhood of the original oil–water contact. To the North of the oil–water contact line, however, some scattered high-amplitude values can be observed on the fluid-saturation attribute map (Figure 11). This is in the water zone, so these anomalies are probably not real and must be attributed to leakage between the pressure and the saturation cubes.

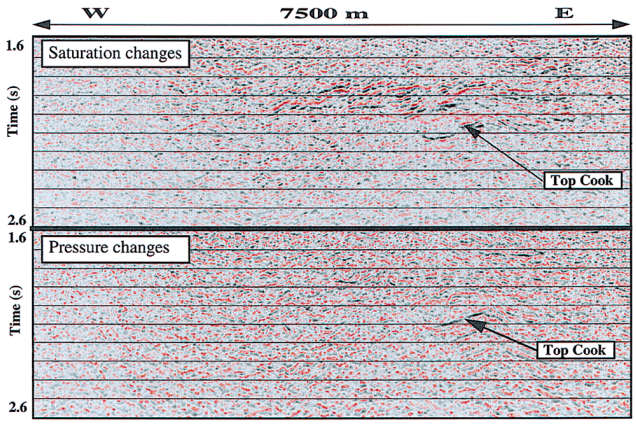

FIG. 7. Estimated changes in oil saturation (top) and pore pressure (bottom) for in-line 2760. The pressure anomaly at the top of the Cook is shown in Figure 10.

DISCUSSION

From the Magnus 4-D study we know that pore-pressure decreases are detectable on time-lapse seismic data (Watts et al., 1996). In the Gullfaks case the pore-pressure increases are more detectable than pore-pressure decreases, which fits well with the velocity–pressure curve in Figure 2. Some leakage between the fluid-saturation change cube and the pressure change

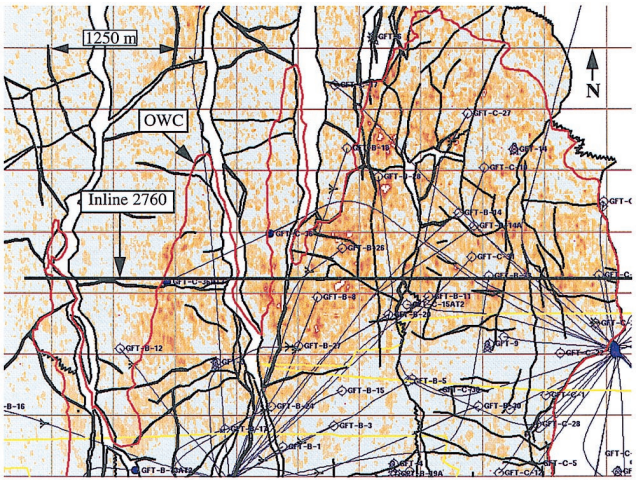

FIG. 8. Map view of the top Brent (top reservoir) interface taken from the saturation-change attribute cube. The original oil–water contact is shown as a red, solid line; the seismic profile shown in Figures 5–7 is also indicated. Hot color is interpreted as areas with high probability of saturation changes close to this interface.

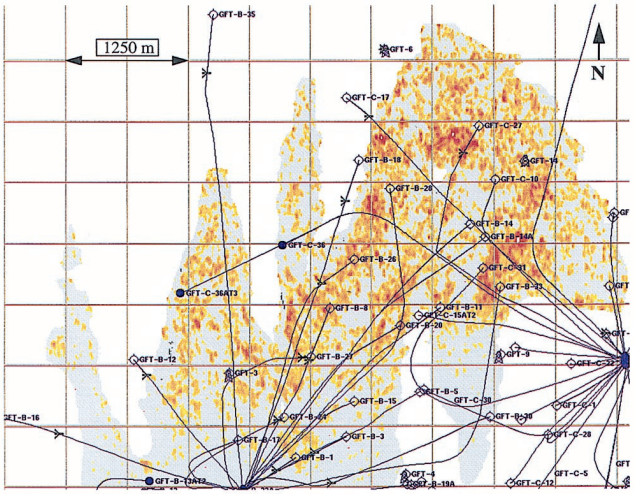

FIG. 9. Time slice through the original oil–water contact taken from the saturation change attribute cube. Hot color is interpreted as areas with high probability of saturation changes close to the original oil–water contact.

cube is observed. This leakage might have several causes: validity of the rock physics model and core measurements, the assumption that the parameters defined in equations (10)–(12) are spatial invariant, uncertainties in the scaling factor between near- and far-offset stacks, or lack of repeatability between the base and monitor surveys. For future improvement, the most crucial issue is to improve repeatability to reduce this leakage problem. Despite leakage problems, the results are encouraging, since the estimated pressure changes fit very well with pressure measurements in wells and the estimated saturation changes fit very well with expected changes (apart from the anomaly to the north).

From an exploration point of view, it is important to notice that the amplitude behavior of seismic data is sensitive to changes in pore pressure and saturation and that the two effects have different AVO behaviors. From Figure 5 we see that the dipping event at the flank of the top Brent structure (marked with arrows on the figure) has a pronounced amplitude increase with offset (1985 data). For the top Cook interface, which has approximately the same dip as the top Brent event,

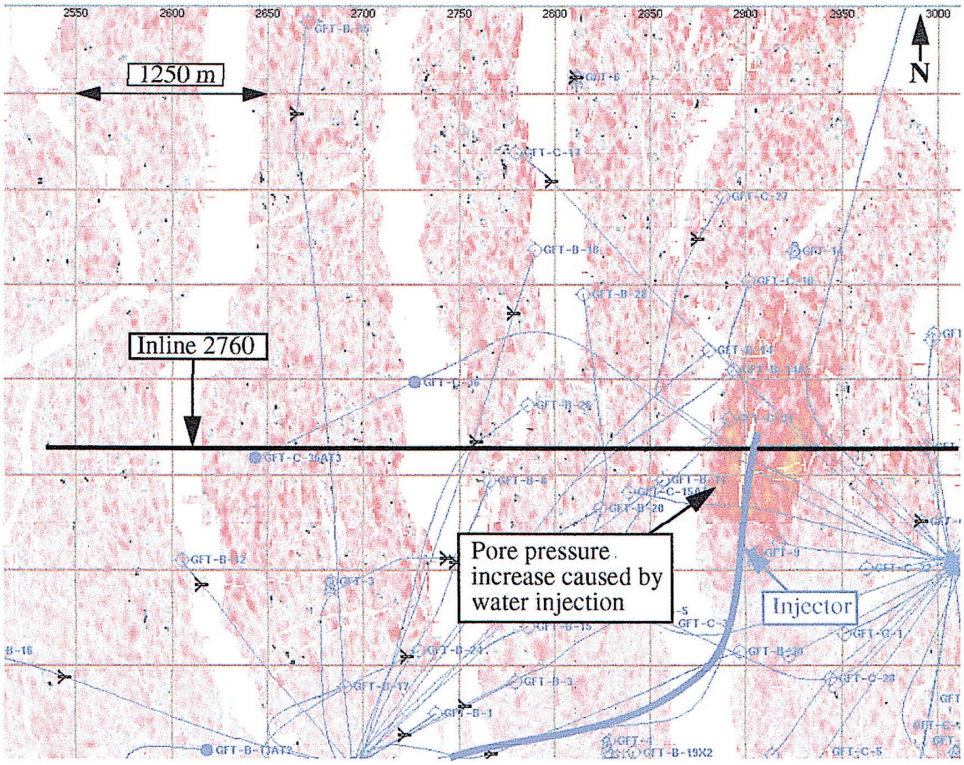

FIG. 10. Map view of the top Cook interface taken from the pressure-change attribute cube. Hot color is interpreted as areas with high probability of pressure changes close to this interface. The pressure anomaly on this map is confirmed by well observations in the segment.

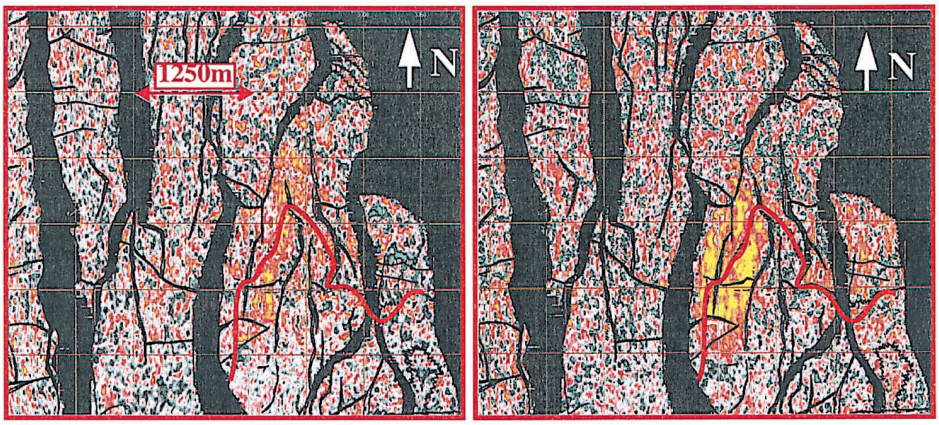

FIG. 11. Comparison of fluid-saturation change attribute map (left) and pore-pressure change attribute map (right) of the top Cook interface. The original oil–water contact is shown in dashed blue lines on both maps. Notice that the pressure anomaly terminates close to faults, while the fluid anomaly terminates close to the original oil–water contact in the western part of this segment.

an amplitude decrease with offset is observed (1996 data). As mentioned above, this segment was overpressured in 1996, and this gives an indication that calibrated AVO analysis might help to distinguish between pressure and fluid effects.

Multicomponent seismic (especially sea-bed seismic) data will probably be a complementary tool to better discriminate between various production effects for future time-lapse seismic projects. It is straightforward to incorporate, for instance, a *PS*-converted stack into the scheme presented here. All computations were done using conventional interactive processing software, and the derived equations were straightforward to implement in such an environment.

CONCLUSIONS

Approximate formulas for computing saturation- and pressure-related changes from time-lapse seismic data have been derived and successfully tested on a time-lapse seismic data set. The formulas are explicit expressions related to near- and far-offset stacks and are therefore well suited for direct implementation in a processing package. Necessary input to obtain the equations is a rock physics model that relates changes in the seismic parameters to changes in pressure and saturation. An interactive processing package was used for all computations.

The method discriminates well between fluid-saturation and pore-pressure changes. Some leakage from the pressure-attribute cube into the saturation-attribute cube are observed. In some areas saturation changes can be observed in the water zone, while well measurements show there have been pressure changes. Fewer leakage problems are observed for the saturation cube into the pressure cube. Both attribute cubes have been a valuable supplement to more conventional time-lapse seismic interpretation techniques.

Finally, it is useful to obtain separate attribute cubes for fluid-saturation and pore-pressure changes. From a reservoir management view, such data cubes are valuable because they can be compared directly with wells observations and extended to areas between wells. This method is therefore a complementary tool for monitoring well performance and planning infill wells in a mature reservoir.

ACKNOWLEDGMENTS

I thank the Gullfaks license group, Norsk Hydro, and Statoil for permission to use the seismic data. I also thank Ivar Brevik and Svein Ellingsrud for valuable input on rock physics, Eilert Hilde for generating map views of the estimated attribute cubes, and Geir Magne Hoddevik for reservoir engineering input. Trine Alsos and Kenneth Duffaut are acknowledged for discussions. Finally, I thank Associate Editor Zhijing Wang and two anonymous reviewers for many constructive comments.

REFERENCES

Bilgeri, D., and Ademeno, E. B., 1982, Predicting abnormally pressured sedimentary rocks: Geophys. Prosp., **30**, 608–621.
Brevik, I., 1999, Rock model based inversion of saturation and pressure changes from time lapse seismic data: 69th Ann. Internat. Mtg., Soc. Expl., Geophys., Expanded Abstracts, 1044–1047.
Gabriels, P. W., Horvei, N. A., Koster, J. K., Onstein, A., and Staples, R., 1999, Time lapse seismic monitoring of the Draugen Field: 69th Ann. Internat. Mtg., Soc. Expl., Geophys., Expanded Abstracts, 2035–2037.
Gassmann, F., 1951, Elastic waves through a packing of spheres: Geophysics, **16**, 673–685.
Landrø, M., 1999, Discrimination between pressure and fluid saturation changes from time lapse seismic data: 69th Ann. Internat. Mtg., Soc. Expl., Geophys., Expanded Abstracts, 1651–1654.
Landrø, M., Solheim, O. A., Hilde, E., Ekren, B. O., and Strønen, L. K., 1999, The Gullfaks 4D seismic study: Petr. Geosci., **5**, 213–226.
Martinez, R. D., Schroeder, J. D., and King, G. A., 1991, Formation pressure prediction with seismic data from the Gulf of Mexico: Form. Eval., **3**, 27–32.
Reynolds, E. B., 1970, Predicting overpressured zones with seismic data: World Oil, **171**, 78–82.
Smith, G. C., and Gidlow, P. M., 1987, Weighted stacking for rock property estimation and detection of gas: Geophys. Prosp., **25**, 993–1014.
Tura, A., and Lumley, D. E., 1998, Subsurface fluid-flow properties form time-lapse elastic-wave reflection data: 43rd Ann. Mtg., SPIE, Proceedings, 125–138.
——— 1999a, Estimating pressure and saturation changes from time-lapse AVO data: 61th Ann. Conf., Eur. Assoc. Geosci. Eng., Extended Abstracts, paper 1–38.
——— 1999b, Estimating pressure and saturation changes from time-lapse AVO data: 69th Ann. Internat. Mtg., Soc. Expl. Geophys., Expanded Abstracts, 1655–1658.
Watts, G. F. T., Jizba, D., Gawith, D. E., and Gutteridge, P., 1996, Reservoir monitoring of the Magnus field through 4D time-lapse seismic analysis: Petr. Geosci., **2**, 361–372.
Winkler, K. W., 1985, Dispersion analysis of velocity and attenuation in Berea Sandstone: J. Geophys. Res., **90**, 6793–6800.

APPENDIX A
SECOND-ORDER APPROXIMATION FOR REFLECTIVITY CHANGE

Assume the *P*-wave velocity in layer 1 (α_1) remains constant between the baseline and the repeated survey as well as for the *S*-wave velocity (β_1) and the density (ρ_1). In layer 2 (which is assumed to be the porous reservoir layer), the preproduction parameters are denoted α_2, β_2, etc. The same parameters after fluid substitution in layer 2 are denoted α_2', $\beta\alpha'_2$, etc. The lithological parameter contrast in *P*-wave velocity is $\Delta\alpha = \alpha_2 - \alpha_1$, while the parameter contrast from fluid changes in layer 2 can be expressed as $\Delta\alpha^F = \alpha_2' - \alpha_2$. The reflection coefficient prior to production is [assuming the Smith and Gidlow (1987) approximation]

$$R_0(\theta) = \frac{1}{2}\left(\frac{\Delta\rho}{\rho} + \frac{\Delta\alpha}{\alpha}\right) - \frac{2\beta^2}{\alpha^2}\left(\frac{\Delta\rho}{\rho} + \frac{2\Delta\beta}{\beta}\right)\sin^2\theta + \frac{\Delta\alpha}{2\alpha}\tan^2\theta, \quad \text{(A-1)}$$

where $\alpha = (\alpha_1 + \alpha_2)/2$, etc. After fluid substitution in layer 2, we find the postproduction reflection coefficient as

$$R_1(\theta) = \frac{1}{2}\left(\frac{\Delta\rho'}{\rho'} + \frac{\Delta\alpha'}{\alpha'}\right) - \frac{2\beta'^2}{\alpha'^2}\left(\frac{\Delta\rho'}{\rho'} + \frac{2\Delta\beta'}{\beta'}\right)\sin^2\theta + \frac{\Delta\alpha'}{2\alpha'}\tan^2\theta. \quad \text{(A-2)}$$

In equation (A-2), $\Delta\alpha' = \alpha_2' - \alpha_1 = \alpha_2 + \Delta\alpha^F - \alpha_1 = \Delta\alpha + \Delta\alpha^F$, etc. Correspondingly, $\alpha' = (\alpha_1 + \alpha_2 + \Delta\alpha^F)/2 = \alpha[1 + (\Delta\alpha^F/2\alpha)]$, etc. Introducing this into equation (A-2), we obtain

$$R_1(\theta) = \frac{1}{2}\left(\left(\frac{\Delta\rho+\Delta\rho^F}{\rho}\right)\left(1-\frac{\Delta\rho^F}{2\rho}\right)+\left(\frac{\Delta\alpha+\Delta\alpha^F}{\alpha}\right)\times\left(1-\frac{\Delta\alpha^F}{2\alpha}\right)\right)-\frac{2\beta^2\left(1+\frac{\Delta\beta^F}{2\beta}\right)^2}{\alpha^2\left(1+\frac{\Delta\alpha^F}{2\alpha}\right)^2}\times\left(\left(\frac{\Delta\rho+\Delta\rho^F}{\rho}\right)\left(1-\frac{\Delta\rho^F}{2\rho}\right)+2\left(\frac{\Delta\beta+\Delta\beta^F}{\beta}\right)\left(1-\frac{\Delta\beta^F}{2\beta}\right)\right)\sin^2\theta+\left(\frac{\Delta\alpha+\Delta\alpha^F}{2\alpha}\right)\left(1-\frac{\Delta\alpha^F}{2\alpha}\right)\tan^2\theta. \quad \text{(A-3)}$$

To second order we obtain

$$R_1(\theta) = R_0(\theta)+\frac{1}{2}\left(\frac{\Delta\rho^F}{\rho}+\frac{\Delta\alpha^F}{\alpha}\right)-\frac{2\beta^2}{\alpha^2}\left(\frac{\Delta\rho^F}{\rho}+\frac{2\Delta\beta^F}{\beta}\right)\sin^2\theta+\frac{\Delta\alpha^F}{2\alpha}\tan^2\theta-\frac{1}{4}\left(\frac{\Delta\rho\Delta\rho^F}{\rho^2}+\frac{(\Delta\rho^F)^2}{\rho^2}+\frac{\Delta\alpha\Delta\alpha^F}{\alpha^2}+\frac{(\Delta\alpha^F)^2}{\alpha^2}\right)-2\frac{\beta^2}{\alpha^2}\left(\frac{\Delta\beta^F}{\beta}\frac{\Delta\rho}{\rho}+\frac{\Delta\beta^F}{\beta}\frac{\Delta\rho^F}{\rho}+\frac{\Delta\beta^F}{\beta}\frac{\Delta\beta}{\beta}+\left(\frac{\Delta\beta^F}{\beta}\right)^2-\frac{\Delta\alpha^F}{\alpha}\frac{\Delta\rho}{\rho}-\frac{\Delta\alpha^F}{\alpha}\frac{\Delta\rho^F}{\rho}-2\frac{\Delta\alpha^F}{\alpha}\frac{\Delta\beta}{\beta}-2\frac{\Delta\alpha^F}{\alpha}\frac{\Delta\beta^F}{\beta}-\frac{\Delta\rho\Delta\rho^F}{2\rho^2}-\frac{(\Delta\rho^F)^2}{2\rho^2}\right)\sin^2\theta-\frac{1}{4}\left(\frac{\Delta\alpha\Delta\alpha^F}{\alpha^2}+\frac{(\Delta\alpha^F)^2}{\alpha^2}\right)\tan^2\theta, \quad \text{(A-4)}$$

which means reflectivity changes including terms to second order can be written

$$\Delta R(\theta) = \frac{1}{2}\left(\frac{\Delta\rho^F}{\rho}+\frac{\Delta\alpha^F}{\alpha}\right)-\frac{2\beta^2}{\alpha^2}\left(\frac{\Delta\rho^F}{\rho}+\frac{2\Delta\beta^F}{\beta}\right)\sin^2\theta+\frac{\Delta\alpha^F}{2\alpha}\tan^2\theta-\frac{1}{4}\left(\frac{\Delta\rho\Delta\rho^F}{\rho^2}+\frac{(\Delta\rho^F)^2}{\rho^2}+\frac{\Delta\alpha\Delta\alpha^F}{\alpha^2}+\frac{(\Delta\alpha^F)^2}{\alpha^2}\right)-2\frac{\beta^2}{\alpha^2}\left(\frac{\Delta\beta^F}{\beta}\frac{\Delta\rho}{\rho}+\frac{\Delta\beta^F}{\beta}\frac{\Delta\rho^F}{\rho}+\frac{\Delta\beta^F}{\beta}\frac{\Delta\beta}{\beta}+\left(\frac{\Delta\beta^F}{\beta}\right)^2-\frac{\Delta\alpha^F}{\alpha}\frac{\Delta\rho}{\rho}-\frac{\Delta\alpha^F}{\alpha}\frac{\Delta\rho^F}{\rho}-2\frac{\Delta\alpha^F}{\alpha}\frac{\Delta\beta}{\beta}-2\frac{\Delta\alpha^F}{\alpha}\frac{\Delta\beta^F}{\beta}-\frac{\Delta\rho\Delta\rho^F}{2\rho^2}-\frac{(\Delta\rho^F)^2}{2\rho^2}\right)\sin^2\theta-\frac{1}{4}\left(\frac{\Delta\alpha\Delta\alpha^F}{\alpha^2}+\frac{(\Delta\alpha^F)^2}{\alpha^2}\right)\tan^2\theta. \quad \text{(A-5)}$$

APPENDIX B
A NUMERICAL EXAMPLE

To test the validity of equation (7), a numerical example is shown in this appendix. Values typical for the cap rock (layer 1) and the reservoir zone (layer 2) at Gullfaks are used. The fluid substituted parameters representing the postproduction case for layer 2 have been estimated using the Gassmann equation. The numerical values for the three seismic parameters are listed in Table B-1.

Inserting the values from Table B-1 into equations (A-1) and (A-2), we find the following reflection coefficients for the pre- and postproduction cases:

$$R_0(\theta) = -0.038 - 0.095\sin^2\theta - 0.026\tan^2\theta, \quad \text{(B-1)}$$

$$R_1(\theta) = 0.043 - 0.083\sin^2\theta + 0.035\tan^2\theta. \quad \text{(B-2)}$$

The exact change in reflectivity from production is therefore $\Delta R^F = R_1 - R_0$:

$$\Delta R^F(\theta) = 0.081 + 0.013\sin^2\theta + 0.061\tan^2\theta. \quad \text{(B-3)}$$

Using the lowest order approximation to ΔR as expressed in equation (7) yields

$$\Delta R^F(\theta) = 0.084 + 0.063\tan^2\theta, \quad \text{(B-4)}$$

which means that the deviation between the two ways of estimating the change in reflectivity is 4% at zero offset and 1% for an angle of 30°. Using the second-order equation (A-5) instead of the lowest order approximation for ΔR gives exactly the same result as equation (B-3).

Table B-1. Seismic parameters used in the numerical example

Seismic parameter	Layer 1	Layer 2 preprod.	Layer 2 postprod	Average preprod.	Average postprod.	Contrast preprod.	Contrast postprod.
P-wave (m/s)	2000	1900	2147	1950	2074	−100	147
S-wave (m/s)	1000	1100	1078	1050	1088	100	78
Density (g/cm^3)	2.0	1.95	2.03	1.98	2.02	−0.05	0.03